ROYAL SOCIETY
OF CHEMISTRY

PAPER

Check for updates

Supercapacitive performance of a PEDOT⊃metal–porphyrin framework composite in a concentrated aqueous LiClO4 electrolyte

Narhari Sapkota,[a] Plawan Kumar Jha, ID *[a] Anssi Peuronen, ID [a]
Sachin Kochrekar, ID [a] Ermei Mäkilä, ID [b] Carita Kvarnström ID [a] and
Ari Lehtonen ID *[a]

Lanthanide-based metal–porphyrin framework-poly(3,4-ethylenedioxythiophene) (Ln-MPF-PEDOT) materials are largely underexplored for use in supercapacitor applications in concentrated aqueous electrolytes. In this study, we report the successful synthesis of a new three-dimensional neodymium–porphyrin MOF (Nd-MPF), followed by the *in situ* oxidative polymerization of PEDOT within its porous channels. The Nd-MPF exhibits excellent structural stability, retaining its crystallinity and framework integrity throughout the polymerization process. Symmetric PEDOT⊃Nd-MPF electrodes demonstrate a wide electrochemical stability window of 1.6 V in concentrated aqueous LiClO4 electrolyte and deliver a high specific capacitance of 166 mF cm^{-2}. The energy and power densities of the PEDOT⊃Nd-MPF electrode are as high as 29 µWh cm^{-2} and 13 mW cm^{-2}, respectively. Finally, our material retains over 75% of its capacitance after 10 000 continuous galvanostatic charge–discharge cycles, highlighting the potential of PEDOT⊃Nd-MPF as a high-performance supercapacitor electrode material.

1. Introduction

Metal–organic frameworks (MOFs) are porous hybrid materials synthesized from organic linkers and metal ions or clusters.[1] They exhibit several remarkable properties, including high porosity, large surface area, unsaturated and accessible metal coordination sites, structural and compositional tunability, and functional diversity.[2–6] Despite these appealing characteristics, using MOFs in electronic and electrochemical applications remains a challenge, primarily due to their poor electrical conductivity and limited chemical stability under acidic or basic conditions. Several approaches to addressing these challenges have been proposed in recent literature.[7] Approaches such as through-bond, extended conjugation, through-space, redox hopping, and guest-promoted methods enabled the preparation of highly conducting and stable MOFs suitable for electronic and electrochemical applications.[7,8] Moreover, recent studies on conducting polymer⊃MOF have opened new avenues for transforming electrically insulating MOFs into conductive materials without altering their structural frameworks. The resistance of insulating MOFs typically ranges from

10^{10} to 10^{12} Ω, which can be reduced by several orders of magnitude through their integration with conducting polymers.[9] Conducting polymers can either be synthesized inside the accessible pores of the MOF or combined with the MOF *via ex situ* or *in situ* oxidative polymerization methods (conducting polymer⊃MOF).[10] For example, the incorporation of polypyrrole (PPy) into the pores significantly enhanced the conductivities of Zn$_3$(lac)$_2$(pybz)$_2$ and Cd$_2$(NDC)(PCA)$_2$ MOFs to 1.0×10^{-2} S cm^{-1} and $\sim 10^{-3}$ S cm^{-1}, respectively.[9,11] Subsequent studies over the years have, in fact, significantly enriched the library of conducting polymer⊃MOF-based materials. During the incorporation of conducting polymers, the porosity of MOFs is often reduced or even eliminated. Nevertheless, some conducting polymer⊃MOF-based materials tested for energy storage applications, specifically supercapacitors, have demonstrated notable capacitance and stability. For example, the capacitive performance of ZIF-67/PPy tube,[12] ZIF-67 (Co$_3$S$_4$/polyaniline) composite,[13] PPy-Cu-CAT,[14] PPy-NiCo-MOF,[15] ZnO-ZnCo/MOF-PANI composite,[16] PPy-Cu-TCPP,[17] and Ni-TCPP@PVP[18] are noteworthy. Furthermore, a subfamily of MOFs known as metal–porphyrin frameworks (MPFs) exhibit several intriguing properties, including intrinsic redox activity, extended π-conjugation, inherent porosity, high rigidity, exposed active sites, and tuneable metal–ligand coordination environments.[19–21] These characteristics facilitate the integration of conducting polymers into MPFs, resulting in notable

[a] *Department of Chemistry, University of Turku, Turku FI-20014, Finland.*
   E-mail: arileh@utu.fi, plawanjha@gmail.com
[b] *Laboratory of Industrial Physics, Department of Physics and Astronomy, University of Turku, Turku FI-20014, Finland*

supercapacitor performance. For instance, Yao et al. reported a high specific capacitance of 496 F g^{-1} by coating Cu-TCPP with polypyrrole (PPy).[17] Similarly, Namratha et al. achieved capacitance values of 205 C g^{-1} and 98 C g^{-1} for Ni-TCPP@PVP and Zn-TCPP MOFs, respectively.[18] Gao et al. reported a capacitance of 210 mAh g^{-1} for the CuDEPP MOF,[22] while Zhou et al. obtained a value of 143 mAh g^{-1} for the CuFNT MOF synthesized via electrochemical oxidative polymerization.[23] Apart from d-block transition metal-based MPFs, lanthanide-based conducting polymer⊃MPFs also have the potential to exhibit excellent supercapacitive performance. Lanthanide MPFs (Ln-MPFs) possess unique properties due to the variable coordination numbers of Ln (CN = 6–12), greater ionic character, and flexible coordination environments.[24] Ln-MPFs are high-coordination-number porous materials with diverse structural topologies. Although many Ln-MPFs have been reported, which display potential for various applications, only a handful have been tested for energy storage in aqueous electrolytes, and reports on the supercapacitive applications of conducting polymer⊃Ln-MPF in concentrated aqueous electrolytes are even rarer.[25]

Here, we synthesized a lanthanide-based metal–porphyrin framework and enhanced its electrical conductivity by incorporating PEDOT into its intrinsic pores. The resulting composite was evaluated as an electrode material for supercapacitor applications. To begin with, we chose Nd^{3+} as the metal ion and synthesized a new three-dimensional Nd-MPF where TCPP-FeCl was used as the linker and benzoic acid as an auxiliary ligand. The accessible intrinsic porosity of the Nd-MPF was then utilized to synthesize PEDOT, thereby transforming the electrically insulating Nd-MPF into a conducting material (PEDOT⊃Nd-MPF). PEDOT is a low-cost, biocompatible, redox-active, and environmentally stable conducting polymer. In addition to its applications in electronics and optoelectronics, PEDOT has been widely recognized in the field of energy storage, specifically supercapacitor.[26] It can be synthesized through various chemical and electrochemical methods. In this study, we employed a chemical oxidative polymerization approach to grow PEDOT directly inside the pores of the Nd-MPF. PEDOT⊃Nd-MPF was further evaluated for symmetric supercapacitor applications.

2. Experimental

2.1. Materials

Neodymium(III) nitrate hexahydrate, N,N-dimethylformamide (DMF), diethyl ether, methyl 4-formylbenzoate, benzoic acid, iodine, and anhydrous lithium perchlorate were purchased from Merck and were used without further purification. 3,4-Ethylenedioxythiophene (EDOT, >98%) and N-methyl-2-pyrrolidone (NMP, >99%) were purchased from TCI chemicals. Pyrrole was purchased from Merck and was distilled before use. 5,10,15,20-Tetrakis(4-carboxyphenyl) porphyrin-FeCl (TCPP-FeCl) linker was prepared using previously reported procedures.[27]

2.2. Synthesis of Nd-MPF

In a Pyrex tube, 0.028 mmol (25 mg) of TCPP-FeCl, 0.17 mmol (76 mg) of Nd(NO$_3$)$_3$·6H$_2$O and 2.7 g of benzoic acid were dissolved in 8 mL of DMF by sonication. Solution was then transferred in a 20 mL poly(tetrafluoroethylene)-lined steel reactor and incubated at 120 °C for 48 h. The resulting mixture was slowly cooled to room temperature (RT). Dark red needle-shaped crystals were collected, washed three times with DMF, and subjected to solvent exchange by immersing them in chloroform for 3 days (chloroform was replaced every 12 h). The crystals were then thermally activated under vacuum at 130 °C for 12 h.

2.3. Preparation of PEDOT⊃Nd-MPF

Approximately 300 mg of pristine Nd-MPF was put in the round-bottom flask and desolvated at 130 °C under vacuum. Subsequently, the Nd-MPF was immersed in diluted EDOT (63 µl of EDOT in 10 ml of diethyl ether) for 48 h, followed by removal of excess monomers under vacuum. The EDOT-loaded Nd-MPF was then exposed to I$_2$ vapours at 90 °C for 48 h. The resulting black material was washed with acetone, deionized water, and hexane to eliminate excess iodine and oligomers.[28] For comparison, polypyrrole⊃Nd-MPF (Ppy⊃Nd-MPF) was synthesized using an identical procedure.

2.4. Characterizations

Single crystal X-ray diffraction data were collected by Rigaku MicroMax-HF generator producing monochromatized Cu Kα radiation and HyPix-6000HE detector. Data collection and reduction were done using the CrysAlisPro software.[29] Crystal structures were solved and refined using SHELXT[30] and SHELXL[31] programs employing the Olex interface.[32] Raman spectroscopy was performed using a Renishaw inVia confocal Raman microscope with a 532 nm diode laser. The PXRD data were collected by Panalytical Aeris Research Edition powder X-ray diffractometer with Bragg–Brentano geometry equipped with PIXcel^{1D} detector using Cu K$_{\alpha1,\alpha2}$ radiation ($\lambda_{\alpha1}$ = 1.5406 Å, $\lambda_{\alpha2}$ = 1.5444 Å). The samples were prepared on a zero background Si disc and rotated at 60 rpm during data collection and the Pawley fitting of the PXRD data was carried out using the Panalytical HighScore Plus software.[33] Thermal analyses were conducted using a TA Instruments SDT Q600 simultaneous TGA-DSC system over a temperature range of 30–1000 °C under a nitrogen atmosphere, with samples placed in aluminium oxide pans. A constant nitrogen flow rate of 50 mL min^{-1} and a heating rate of 10 °C min^{-1} were maintained throughout the measurements. Argon and krypton adsorption isotherms were recorded at –196 °C using a 3Flex 3500 instrument (Micromeritics Corp., USA). The apparent specific surface area was determined using the Brunauer–Emmett–Teller (BET) method. Pore volume was estimated based on the Gurvich rule, using the total adsorbed amount at the isotherm's uptake plateau. Pore size distribution was calculated with MicroActive v5.01 software (Micromeritics Corp.) employing density functional theory (DFT) with a zeolite model, assuming cylindrical pore geometry. Before the adsorption experiments, the samples were degassed at

120 °C for 2 h followed by 12 h at 60 °C in VacPrep 061 (Micromeritics Corp.) using a scroll vacuum pump. Prior to the measurement, the samples were further outgassed *in situ* for 2 h at 120 °C in the 3Flex instrument under turbomolecular vacuum pump. Field emission scanning electron microscopy (FE-SEM) images and energy-dispersive X-ray spectra (EDS) of powder samples were collected using Thermo Scientific Apreo S instrument, equipped with Oxford Instruments UltimMax 100 EDS spectrometer. X-ray photoelectron spectroscopy (XPS) measurements were performed with Thermo Scientific Nexsa instrument using monochromatized Al Kα (1486.7 eV) source. Four-probe current–voltage ($I–V$) measurements were performed on a pressed pellet (5 ton) using Keithley 2460 Source Meter. Electrochemical studies were carried out using Iviumstat (IVIUM) and BioLogic VSP-300 Galvanostat/Potentiostat workstations.

2.5. Electrochemical characterization

To prepare the ink for active electrodes, 80 wt% active material, 10 wt% conductive carbon, and 10 wt% Nafion solution were mixed in 0.3 mL of NMP. Approximately 2 mg of the resulting ink was drop casted onto a 1 cm^2 graphite sheet and dried in an oven at 90 °C for 10 h. The electrodes were then pressed under high pressure ($\sim$0.5 ton) prior to electrochemical characterization. All electrochemical characterizations were performed in a symmetric 2-electrode setup in aqueous 5.6 m LiClO$_4$ electrolyte solutions.

3. Results and discussions

Nd-MPF was synthesized using solvothermal process (Fig. 1a) and isolated as dark red needle-shaped crystals. The single crystal X-ray structure determination showed that Nd-MPF crystallized in a monoclinic crystal system with the space group $C2/c$ (Fig. 1b). Each Nd^{3+} ion in the structure is coordinated by four carboxylic O donor atoms from four porphyrin linkers (two carboxylic acid groups in porphyrin are coordinated from horizontal side and two are coordinated from vertical side; Nd–O distances within 2.35–2.40 Å), three O donor atoms from
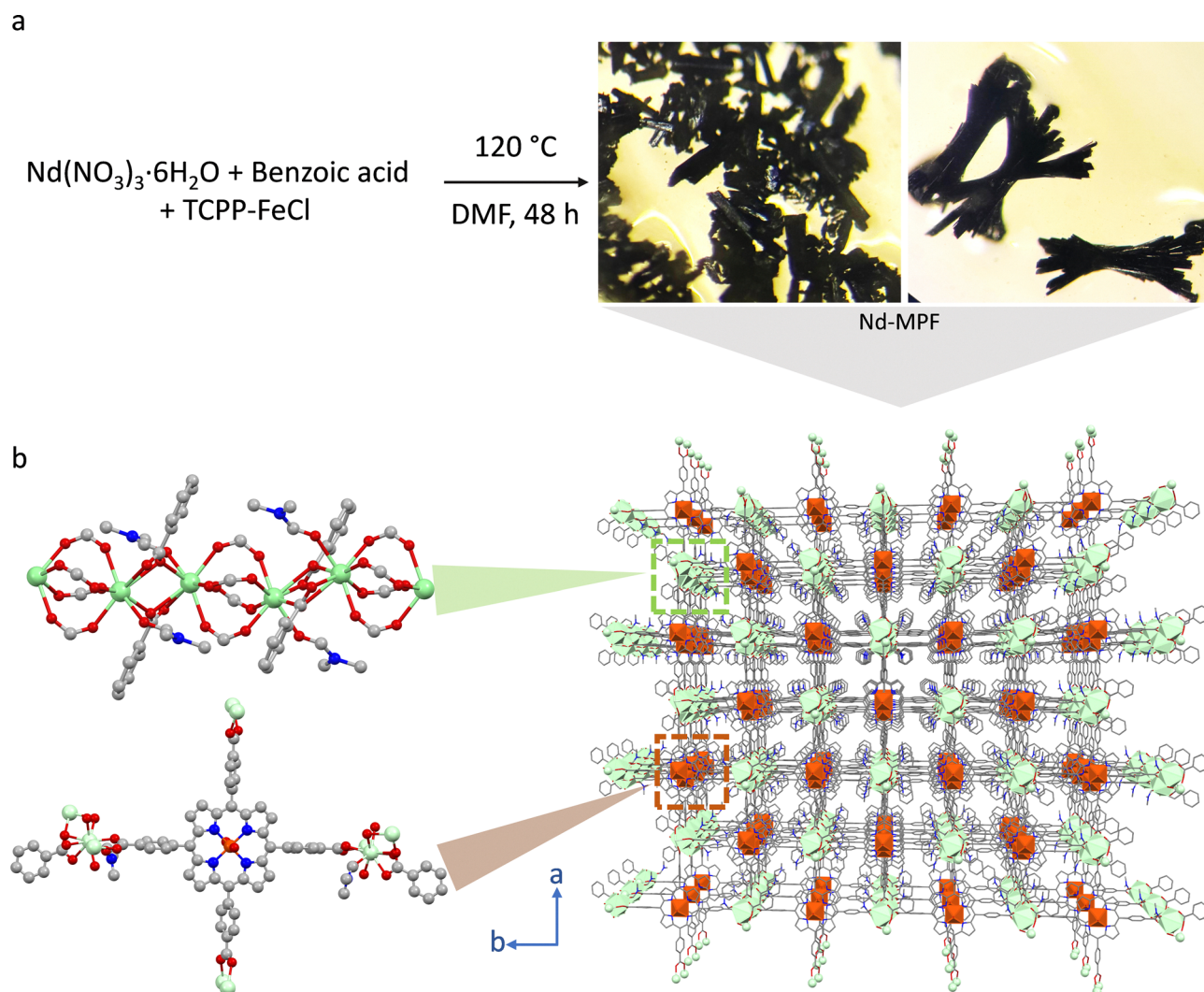

Nd(NO$_3$)$_3$·6H$_2$O + Benzoic acid + TCPP-FeCl

120 °C
DMF, 48 h

Nd-MPF

Fig. 1 (a) Schematic of solvothermal synthesis (left) and resulted crystals of Nd-MPF (right), and (b) 3D framework of Nd-MPF (right) and asymmetric unit of Nd-MPF (left). Colour code: light green – Nd; orange – Fe; grey & dark grey – C; red – O; blue – N.

two benzoate ligands (Nd–O distances within 2.46–2.64 Å) and one O donor atom from DMF (Nd–O distance 2.44 Å) giving a total coordination number eight and a square antiprismatic coordination geometry as confirmed by calculation of continuous shape measures using Shape program.[34] Both chelating benzoate ligands and porphyrin linkers are coordinated to the Nd centres in bridging mode and thus form a one-dimensional chain along the crystallographic *b*-axis. Porphyrin carboxylate groups are coordinated to the chain along the *a*- and *c*-axis directions thereby providing a three-dimensional network

(Fig. 1b). Based on the Fe–O distances (2.11 Å) the iron in the porphyrin core is coordinated to two water molecules in addition to the four porphyrin N atoms.

The intrinsic porosity and wide pore diameter of Nd-MPF make it an ideal host for accommodating EDOT monomers for subsequent in-pore polymerization into PEDOT. In this approach, Nd-MPF was soaked in liquid EDOT for a specific time, followed by vacuum drying to remove excess, unwanted EDOT monomers (Fig. 2a). The loaded EDOT was then polymerized using iodine as an oxidant. The structural integrity of
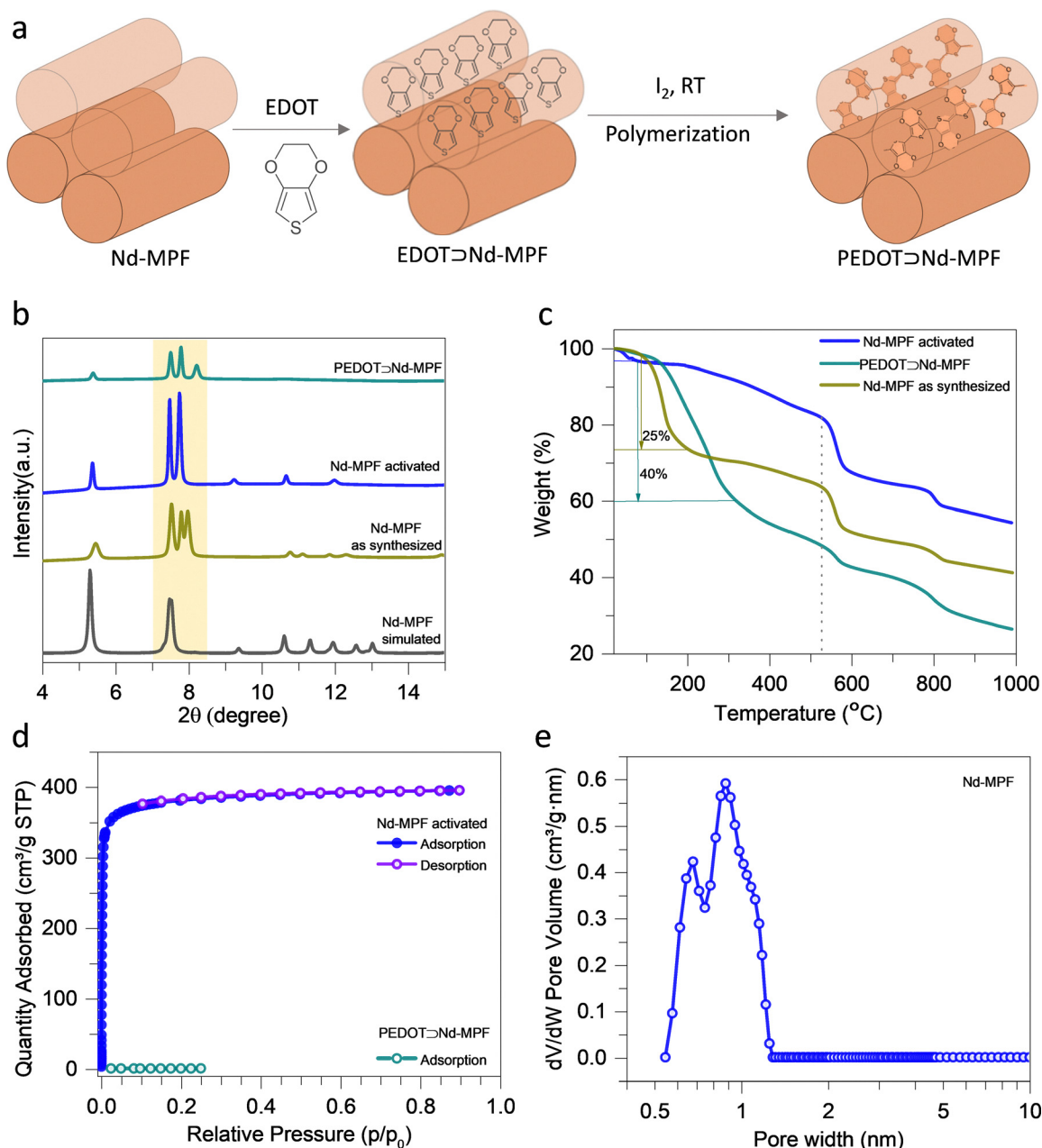

Fig. 2 (a) Schematic of incorporation of EDOT into the pores of Nd-MPF and subsequent polymerization using iodine at RT, (b) PXRD patterns of Nd-MPF simulated from SCXRD data, as synthesized Nd-MPF, activated Nd-MPF, and PEDOT⊃Nd-MPF, (c) TGA of Nd-MPF, activated Nd-MPF, and PEDOT⊃Nd-MPF, (d) Ar adsorption–desorption isotherm of activated Nd-MPF with Kr adsorption–desorption isotherm of PEDOT⊃Nd-MPF at 196 K, and (e) pore size distribution of Nd-MPF.

the Nd-MPF framework following PEDOT polymerization was confirmed using PXRD. As shown in Fig. 2b, the diffraction pattern of the as-synthesized compound aligns well with the simulated pattern obtained from single-crystal diffraction data. Notably, in the as-synthesized Nd-MPF, a peak observed around $2\theta = 8°$ most likely corresponds to periodically arranged solvent (DMF) molecules, which disappears after the activation process (Nd-MPF activated), indicating the removal of guest molecules. Notably, after the incorporation of PEDOT, this peak reappears at a slightly shifted position ($2\theta = 8.2°$), suggesting that PEDOT chains are periodically organized within the channels of the

Nd-MPF (Fig. 2b). This suggests PEDOT is confined and ordered within the intrinsic pore structure, without compromising the crystallinity of Nd-MPF.

Thermogravimetric analysis (TGA) was employed to evaluate the thermal stability of PEDOT⊃Nd-MPF and to estimate the amount of incorporated PEDOT (Fig. 2c). The as-synthesized Nd-MPF exhibited approximately 25% weight loss due to the presence of guest DMF molecules. After an initial ∼5% weight loss attributed to residual solvent, the activated Nd-MPF showed an additional ∼10% weight loss up to 525 °C, corresponding to framework decomposition. In contrast,
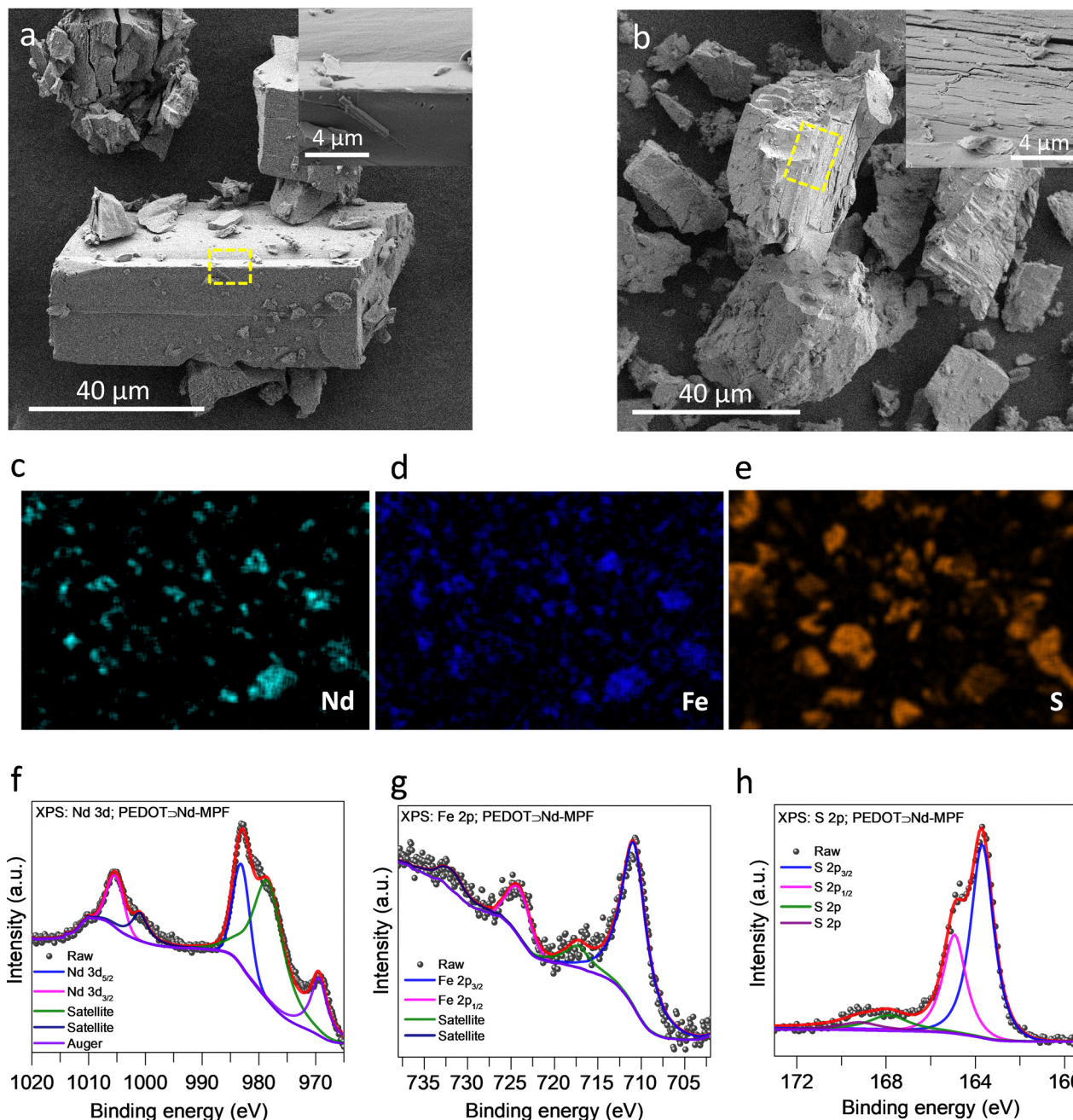

Fig. 3 (a) FESEM image of Nd-MPF (inset: zoomed-in image), (b)–(e) FESEM image and EDXS mapping of PEDOT⊃Nd-MPF (inset: zoomed-in image), and (f)–(h) Nd 3d, Fe 2p, and S 2p XPS plots of PEDOT⊃Nd-MPF.

PEDOT⊃Nd-MPF displayed a ∼40% weight loss up to 275 °C, followed by a total weight loss of ∼52% by 525 °C. Based on the differential weight loss compared to the pristine Nd-MPF, the PEDOT loading in the Nd-MPF is estimated to be approximately 30–35 wt%. Argon adsorption–desorption measurements revealed that the Nd-MPF exhibits a characteristic Type I isotherm, indicative of a microporous material, with a steep Ar uptake filling the pores at low relative pressures (Fig. 2d).[35] The apparent surface area (SA), calculated using the BET method,[36] is approximately 1300 m^2 g^{-1}. Density functional theory (DFT) analysis using a zeolite kernel estimated the pore size distribution to be in the range of 0.8–1.1 nm (Fig. 2e). In contrast, the PEDOT-loaded Nd-MPF displayed a significantly reduced surface area of approximately 1.0 m^2 g^{-1} (Fig. 2d). The combined results from TGA and gas adsorption analyses strongly suggest that the pores of the Nd-MPF are almost entirely filled with PEDOT polymer chains.

The morphology and elemental composition of Nd-MPF and PEDOT⊃Nd-MPF powders were investigated using FE-SEM, EDX, and XPS. The SEM images of both the materials revealed that the block-like morphology of Nd-MPF remained intact throughout the rigorous *in situ* polymerization of PEDOT within the pores (Fig. 3a and b), which is consistent with the PXRD results (Fig. 2b). Notably, there was no evidence of surface-adhered, randomly polymerized PEDOT (Inset: Fig. 3a and b), which implies that the 30–35% weight loss observed in TGA is primarily due to PEDOT confined within the Nd-MPF channels. Elemental analysis of PEDOT⊃Nd-MPF showed the presence of all the expected elements in Nd-MPF and the composite, affirming the successful polymerization of PEDOT (Fig. S2). The elemental maps obtained by EDS for the EDOT⊃Nd-MPF and PEDOT⊃Nd-MPF samples showed that sulphur was uniformly distributed along with Fe, Nd, N, and O, indicating the presence of the EDOT monomer and PEDOT in Nd-MPF, respectively (Fig. 3c–e and Fig. S3, S4). In the Raman spectra, a peak centred at approximately 1441 cm^{-1} corresponds to the $C_\alpha=C_\beta(-O)$ symmetric stretching mode (Fig. S5). This peak indicates a high level of doping in the PEDOT backbone of PEDOT⊃Nd-MPF and further confirms the efficient *in situ* polymerization of EDOT into PEDOT.

Similarly, the XPS survey spectrum confirmed the presence of all expected elements in both the materials (Fig. S4a). High-resolution XPS spectra of PEDOT⊃Nd-MPF for the Nd 3d, Fe 2p, and S 2p regions are shown in Fig. 3f–h. The fitted Nd 3d spectrum displays a characteristic doublet at approximately 983.1 eV and 1005.4 eV, corresponding to Nd $3d_{5/2}$ and Nd $3d_{3/2}$, respectively, along with two satellite peaks, confirming the presence of Nd in its expected oxidation state (*i.e.* Nd(III)) (Fig. 3f).[37] Additionally, a peak at around 969.3 eV is attributed to an Auger transition of Nd(III). The Fe 2p spectrum exhibits a doublet centred at approximately 711 eV (Fe $2p_{3/2}$) and 724.4 eV (Fe $2p_{1/2}$), accompanied by satellite features, indicating the presence of Fe(II) in the porphyrin core of the Nd-MPF (Fig. 3g). In the S 2p region, a doublet at around 163.7 eV and 164.9 eV, corresponding to S $2p_{3/2}$ and S $2p_{1/2}$, respectively, confirms the incorporation of PEDOT (Fig. 3f). This is further supported by the C 1s and O 1s XPS spectra (Fig. S6b and c).

After a successful *in situ* polymerization of PEDOT within the pores of the Nd-MPF, the electrical conductivity of the composite was evaluated using a four-probe *I–V* measurement on a pressed pellet (Fig. 4). The resistance of Nd-MPF exceeded the measurement limits of the instrument. The conductivity of the PEDOT⊃Nd-MPF was approximately 0.017 S cm^{-1}, significantly higher than that of the pristine Nd-MPF. The high conductivity, combined with chemical characteristics of PEDOT⊃Nd-MPF, underscores its significance as an active electrode material for supercapacitor applications. For comparison, the formation of polypyrrole within the pores of the Nd-MPF MOF was studied through *in situ* polymerization of pyrrole. Conductivity was measured using the four-probe method, revealing that the conductivity of PPy⊃Nd-MPF (0.0016 S cm^{-1}) is significantly lower than that of PEDOT⊃Nd-MPF (0.017 S cm^{-1}). The four-probe *I–V* characteristics of PPy⊃Nd-MPF are shown in the supplementary material (Fig. S10).

The supercapacitive performance of Nd-MPF and PEDOT⊃Nd-MPF was evaluated using a symmetric two-electrode configuration in aqueous 5.6 m $LiClO_4$ electrolyte. Cyclic voltammetry (CV), galvanostatic charge–discharge (GCD), and electrochemical impedance spectroscopy (EIS) were employed for electrochemical characterization (Fig. 5 and Fig. S7). The partially rectangular shape of the CV curve for both the materials indicates a predominant electric double-layer capacitance (EDLC) behaviour at the electrode–electrolyte interface, which is further supported by the partial-triangular shape of the GCD curves (Fig. 5a and b).[38] Notably, we achieved a wide electrochemical stability window of 1.6 V for both the materials in a concentrated aqueous 5.6 m $LiClO_4$ electrolyte, which, to the best of our knowledge, has rarely been observed for any lanthanide-MPF–PEDOT-based materials. The EDLC nature was maintained across a wide range of scan rates (5–200 mV s^{-1}) and current densities (0.4–20 mA cm^{-2}) (Fig. S7). PEDOT⊃Nd-MPF exhibited
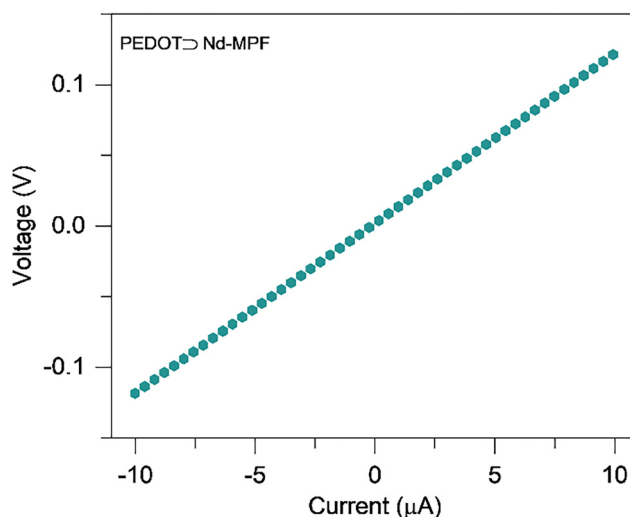

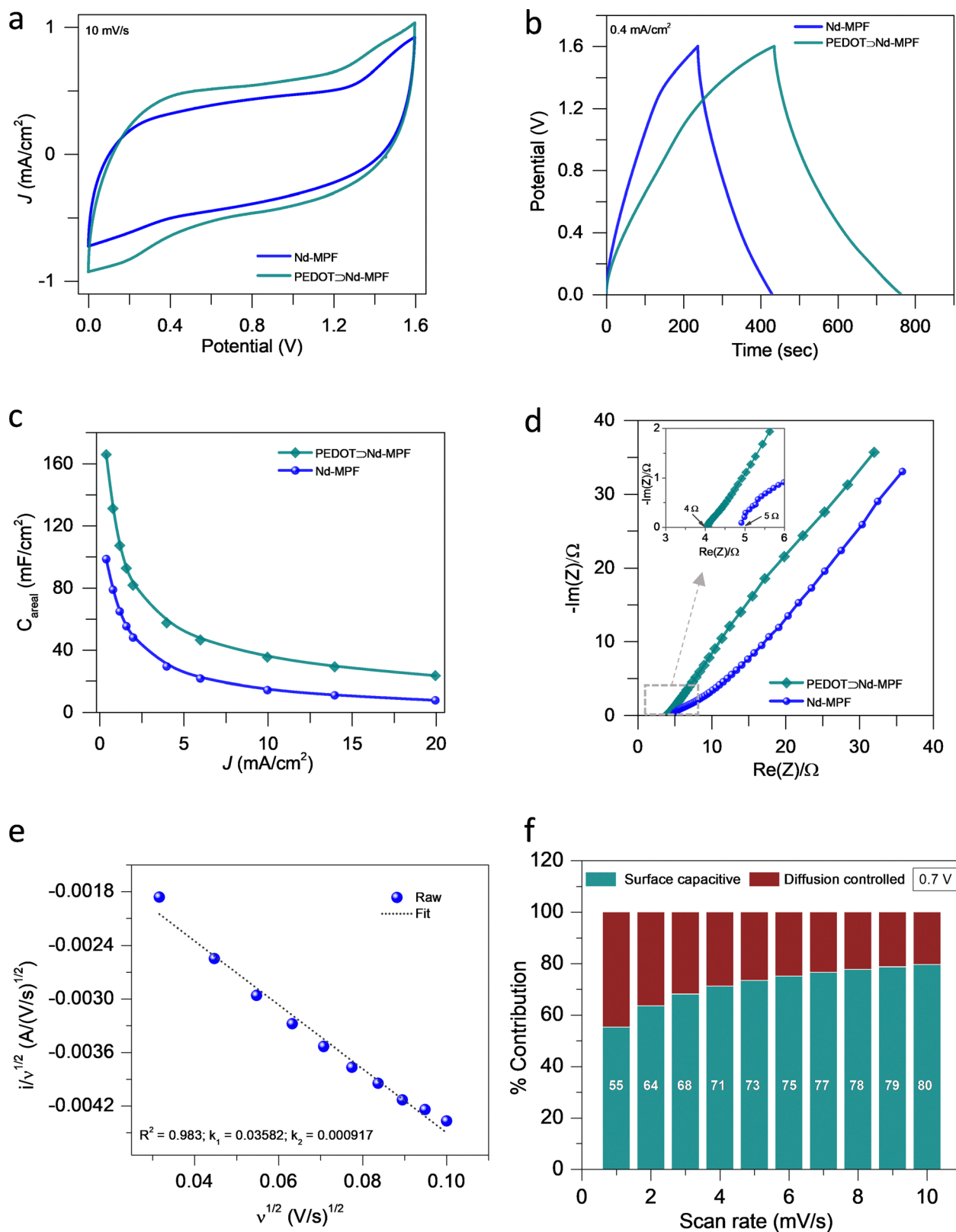Fig. 4 Four probe *I–V* characteristics of PEDOT⊃Nd-MPF.

Fig. 5 (a) CV, (b) GCD, (c) Specific capacitance *vs.* current density plot, (d) Nyquist plot (inset: Zoomed-in at a high frequency region), (e) k_1 and k_2 determination, and (f) % contribution of surface capacitance and diffusion-controlled processes at a potential of 0.7 V and scan rates of 1–10 mV s^{-1}, respectively.
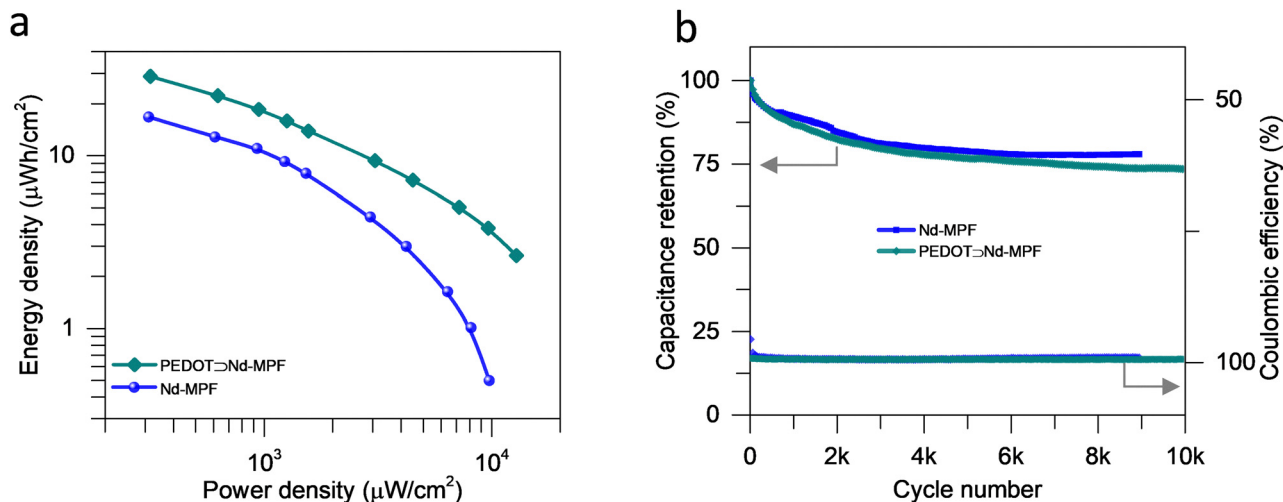
Fig. 6 (a) Ragone plot, and (b) stability tests of Nd-MPF and PEDOT⊃Nd-MPF.

a larger area under the CV and longer discharge time in the GCD curves compared to Nd-MPF, indicating enhanced charge storage capability (Fig. 5a and b). The specific capacitance values of both the materials were calculated using the formula appropriate for materials exhibiting EDLC characteristics (SI). Furthermore, the capacitance of PEDOT⊃Nd-MPF was calculated to be approximately 166 mF cm^{-2} at a current density of 0.4 mA cm^{-2}, which is about 1.7 times higher than that of pristine Nd-MPF (96 mF cm^{-2}) (Fig. 5c). This value is among the highest reported for conducting polymer⊃MOF/ MPF composites tested in aqueous electrolytes (Table S3). The enhanced capacitance is primarily attributed to the periodically arranged conducting PEDOT network within the porous MPF's channels. The improved electrical conductivity was further supported by EIS (Fig. 5d). The equivalent series resistance (ESR) derived from the Nyquist plot was approximately 4 Ω for PEDOT⊃Nd-MPF, which is lower than that of the pristine Nd-MPF ($\sim$5 Ω). This indicates that ion–electrode interactions are more facile in the former than the latter (see Fig. 5d, inset). Notably, the Nyquist plot of the composite did not display a prominent semicircle, whereas a partial semicircle was observed for Nd-MPF, indicating a higher charge-transfer resistance at the electrode–electrolyte interface in the latter compared to composite (Fig. 5d: inset). The better capacitive behaviour of the composite can be seen from the Nyquist curve at a lower frequency region (Fig. 5d), complementing the capacitance values obtained from the GCD analysis.[39]

The charge storage process is dominated by either surface-capacitive or diffusion-controlled mechanisms, which can be determined using the Dunn method.[40] The percentage contributions of the diffusion-controlled and surface-capacitive processes were calculated using the equation $i(V) = k_1 v + k_2 v^{1/2} = i_{\text{diffusion controlled}} + i_{\text{surface capacitive}}$ (Fig. 5e, f, and Fig. S8). Furthermore, at a potential of 0.7 V, the contribution from the surface-capacitive process was found to be 55–80% at scan rates ranging from 1 to 10 mV s^{-1}, suggesting that an EDLC-dominated

process occurs at the electrode–electrolyte interface (Fig. 5f and Fig. S8).

A physical mixture of PEDOT (30%) and Nd-MPF (70%) was prepared, and its capacitance was compared with that of PEDOT⊃Nd-MPF (Fig. S9). The physical mixture exhibited a lower capacitance than the *in situ* polymerized material.

The current era of energy consumption demands materials with high energy (E_d) and power (P_d) densities, along with long-term charge–discharge stability. The specific E_d and P_d values of PEDOT⊃Nd-MPF are as high as 29 μWh cm^{-2} and 13 mW cm^{-2}, respectively, which are approximately 1.7 and 1.3 times higher than those of pristine Nd-MPF, indicating the constructive effect of PEDOT within the pores (Fig. 6a). Finally, more than 75% of the initial capacitance was retained in Nd-MPF and PEDOT⊃Nd-MPF materials, after 9000 and 10 000 GCD cycles, respectively, at a current density of 10 mA cm^{-2} (Fig. 6b). This result highlights the robustness of Nd-MPF for both successful *in situ* polymerization and prolonged cycling stability.

4. Conclusion

A new three-dimensional Nd-MPF was synthesised using Nd^{3+} ion, a TCPP-FeCl linker and benzoic acid as an auxiliary ligand. The intrinsic pores of the Nd-MPF (SA = 1300 m^2 g^{-1}) were then utilised for the *in situ* polymerisation of the conducting polymer PEDOT. The conducting PEDOT⊃Nd-MPF (0.017 S m^{-1}) was tested as an active electrode for supercapacitor applications. The symmetric supercapacitor of PEDOT⊃Nd-MPF exhibited remarkable capacitance performance of approximately 166 mF cm^{-2} in a concentrated aqueous electrolyte, which is 1.7 times higher than that of pristine Nd-MPF. To the best of our knowledge, this is the first report in which a wide electrochemical stability window of 1.6 V has been achieved for any Ln-MPF–PEDOT supercapacitor. Finally, the capacitance retention of PEDOT⊃Nd-MPF was found to be $\sim$75% after 10 000 cycles.

Author contributions

Narhari Sapkota – writing original draft, visualization, methodology, investigation, formal analysis, conceptualization. Plawan Kumar Jha – writing original draft, investigation, formal analysis, conceptualization, co-supervision. Anssi Peuronen – writing review & editing, investigation, formal analysis, Co-supervision. Sachin Kochrekar – investigation, formal analysis. Ermei Mäkilä – formal analysis. Carita Kvarnström – formal analysis. Ari Lehtonen – writing review & editing, supervision, resources, project administration.

Conflicts of interest

The authors declare no competing financial interest.

Data availability

The data supporting this article have been included as part of the supplementary information (SI). Supplementary information containing PXRD patterns, EDS spectra, XPS spectra and electrochemical analyses is available. See DOI: **https://doi.org/10.1039/d5tc03251b**.

CCDC 2478823 contains the supplementary crystallographic data for this paper.[41]

Acknowledgements

References

1 H. C. Zhou, J. R. Long and O. M. Yaghi, *Chem. Rev.*, 2012, **112**, 673–674.

2 I. M. Hönicke, I. Senkovska, V. Bon, I. A. Baburin, N. Bönisch, S. Raschke, J. D. Evans and S. Kaskel, *Angew. Chem., Int. Ed.*, 2018, **57**, 13780–13783.

3 O. K. Farha, I. Eryazici, N. C. Jeong, B. G. Hauser, C. E. Wilmer, A. A. Sarjeant, R. Q. Snurr, S. T. Nguyen, A. Ö. Yazaydın and J. T. Hupp, *J. Am. Chem. Soc.*, 2012, **134**, 15016–15021.

4 Ü. Kökçam-Demir, A. Goldman, L. Esrafili, M. Gharib, A. Morsali, O. Weingart and C. Janiak, *Chem. Soc. Rev.*, 2020, **49**, 2751–2798.

5 D. Huang, G. Wang, M. Cheng, G. Zhang, S. Chen, Y. Liu, Z. Li, W. Xue, L. Lei and R. Xiao, *Chem. Eng. J.*, 2021, **421**, 127817.

6 L. Jiao, J. Y. R. Seow, W. S. Skinner, Z. U. Wang and H.-L. Jiang, *Mater. Today*, 2019, **27**, 43–68.

7 L. S. Xie, G. Skorupskii and M. Dincă, *Chem. Rev.*, 2020, **120**, 8536–8580.

8 S. Tao, J. Wang and J. Zhang, *ACS Nano*, 2025, **19**, 9484–9512.

9 B. Dhara, S. S. Nagarkar, J. Kumar, V. Kumar, P. K. Jha, S. K. Ghosh, S. Nair and N. Ballav, *J. Phys. Chem. Lett.*, 2016, **7**, 2945–2950.

10 H. Meng, Y. Han, C. Zhou, Q. Jiang, X. Shi, C. Zhan and R. Zhang, *Small Methods*, 2020, **4**, 2000396.

11 Q. Wang and C. Zhang, *Macromol. Rapid Commun.*, 2011, **32**, 1610–1614.

12 X. Xu, J. Tang, H. Qian, S. Hou, Y. Bando, Md. S. A. Hossain, L. Pan and Y. Yamauchi, *ACS Appl. Mater. Interfaces*, 2017, **9**, 38737–38744.

13 M. Xu, H. Guo, T. Zhang, J. Zhang, X. Wang and W. Yang, *J. Energy Storage*, 2021, **35**, 102303.

14 T. Yue, R. Hou, X. Liu, K. Qi, Z. Chen, Y. Qiu, X. Guo and B. Y. Xia, *ACS Appl. Energy Mater.*, 2020, **3**, 11920–11928.

15 Y. Liu, Y. Wang, Y. Chen, C. Wang and L. Guo, *Appl. Surf. Sci.*, 2020, **507**, 145089.

16 D. Qin, B. Zhou, Z. Li and C. Yang, *J. Mol. Struct.*, 2024, **1309**, 138140.

17 H. Yao, F. Zhang, G. Zhang, H. Luo, L. Liu, M. Shen and Y. Yang, *Chem. Eng. J.*, 2018, **334**, 2547–2557.

18 E. Namratha, T. K. Ghosh, M. S. S. Babu, A. J. M. Reddy, G. R. Rao and K. Suresh, *J. Mater. Sci.: Mater. Electron.*, 2024, **35**, 2034.

19 W. Zhao, W. Wang, J. Peng, T. Chen, B. Jin, S. Liu, W. Huang and Q. Zhao, *Dalton Trans.*, 2019, **48**, 9631–9638.

20 M. Wu, J. Hu, D. Sun, J. Lu, H. Duan and P. Duan, *Microchem. J.*, 2024, **196**, 109622.

21 A. Yao, D. Hua, F. Zhao, D. Zheng, J. Pan, Y. Hong, Y. Liu, X. Rao, S. Zhou and G. Zhan, *Sep. Purif. Technol.*, 2022, **282**, 120022.

22 P. Gao, Z. Chen, Z. Zhao-Karger, J. E. Mueller, C. Jung, S. Klyatskaya, T. Diemant, O. Fuhr, T. Jacob, R. J. Behm, M. Ruben and M. Fichtner, *Angew. Chem.*, 2017, **129**, 10477–10482.

23 J. Zhou, B. Zheng, X. Huang, W. Zhou, C. Sun, X. Sun, T. Zhang, Z. Huang, S. Tan, J. Liu and P. Gao, *Adv. Funct. Mater.*, 2024, **34**, 2411127.

24 N. Sapkota, E. Mäkilä, A. Lehtonen and A. Peuronen, *Cryst. Growth Des.*, 2025, **25**, 3119–3127.

25 L. Niu, T. Wu, M. Chen, L. Yang, J. Yang, Z. Wang, A. A. Kornyshev, H. Jiang, S. Bi and G. Feng, *Adv. Mater.*, 2022, **34**, 2200999.

26 P. K. Jha, S. Kochrekar, A. Jadhav, R. Lassfolk, M. Salomäki, E. Mäkilä and C. Kvarnström, *Energy Storage Mater.*, 2024, **72**, 103758.

27 H.-Q. Xu, J. Hu, D. Wang, Z. Li, Q. Zhang, Y. Luo, S.-H. Yu and H.-L. Jiang, *J. Am. Chem. Soc.*, 2015, **137**, 13440–13443.

28 A. Jadhav, K. Gupta, P. Ninawe and N. Ballav, *Angew. Chem., Int. Ed.*, 2020, **59**, 2215–2219.

29 D. Feng, Z. Gu, J. Li, H. Jiang, Z. Wei and H. Zhou, *Angew. Chem.*, 2012, **124**, 10453–10456.

30 G. M. Sheldrick, *Acta Crystallogr., Sect. A: Found. Crystallogr.*, 2015, **71**, 3–8.

31 G. M. Sheldrick, *Acta Crystallogr., Sect. C: Struct. Chem.*, 2015, **71**, 3–8.

32 O. V. Dolomanov, L. J. Bourhis, R. J. Gildea, J. A. K. Howard and H. Puschmann, *J. Appl. Crystallogr.*, 2009, **42**, 339–341.

33 T. Degen, M. Sadki, E. Bron, U. König and G. Nénert, *Powder Diffr.*, 2014, **29**, S13–S18.

34 M. Llunell, D. Casanova, J. Cirera, P. Alemany and S. Alvarez, *SHAPE, version 2.1*, Universitat de Barcelona, Barcelona, Spain, 2013.

35 M. Thommes, K. Kaneko, A. V. Neimark, J. P. Olivier, F. Rodriguez-Reinoso, J. Rouquerol and K. S. W. Sing, *Pure Appl. Chem.*, 2015, **87**, 1051–1069.

36 J. Rouquerol, P. Llewellyn and F. Rouquerol, *Stud. Surf. Sci. Catal.*, 2007, **160**, 49–56.

37 J. P. Baltrus and M. J. Keller, *Surf. Sci. Spectra*, 2019, **26**, 014001.

38 P. K. Jha, S. K. Singh, V. Kumar, S. Rana, S. Kurungot and N. Ballav, *Chemistry*, 2017, **3**, 846–860.

39 B. A. Mei, O. Munteshari, J. Lau, B. Dunn and L. Pilon, *J. Phys. Chem. C*, 2018, **122**, 194–206.

40 S. Harish and P. U. Sathyakam, *J. Electron. Mater.*, 2025, **54**, 10858–10872.

41 CCDC 2478823: Experimental Crystal Structure Determination, 2025, DOI: **10.5517/ccdc.csd.cc2p6f1d**.